

This is a repository copy of Fully-relativistic electron Bernstein wave current drive simulations in the STEP spherical tokamak.

White Rose Research Online URL for this paper: <a href="https://eprints.whiterose.ac.uk/id/eprint/219592/">https://eprints.whiterose.ac.uk/id/eprint/219592/</a>

Version: Published Version

#### Article:

Biswas, Bodhi orcid.org/0000-0001-7993-3732, Freethy, Simon and Vann, Roddy orcid.org/0000-0002-3105-2546 (2024) Fully-relativistic electron Bernstein wave current drive simulations in the STEP spherical tokamak. Nuclear Fusion. ISSN: 1741-4326

https://doi.org/10.1088/1741-4326/ad8fbc

### Reuse

This article is distributed under the terms of the Creative Commons Attribution (CC BY) licence. This licence allows you to distribute, remix, tweak, and build upon the work, even commercially, as long as you credit the authors for the original work. More information and the full terms of the licence here: https://creativecommons.org/licenses/

#### Takedown

If you consider content in White Rose Research Online to be in breach of UK law, please notify us by emailing eprints@whiterose.ac.uk including the URL of the record and the reason for the withdrawal request.





**PAPER • OPEN ACCESS** 

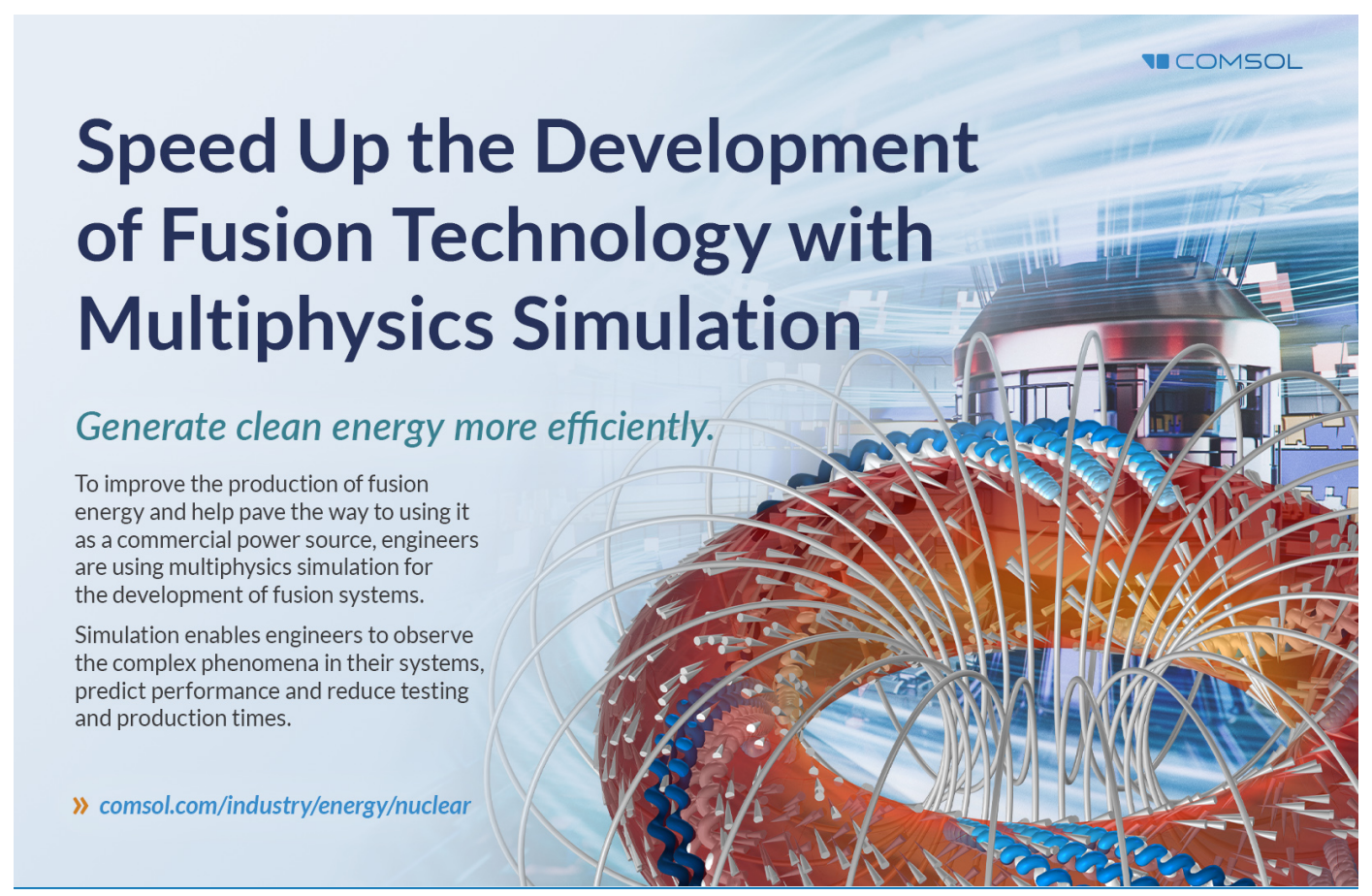
# Fully-relativistic electron Bernstein wave current drive simulations in the STEP spherical tokamak

To cite this article: Bodhi Biswas et al 2025 Nucl. Fusion 65 016010

View the article online for updates and enhancements.

# You may also like

- Split string field theory II
  David J. Gross and Washington Taylor
- Generalised T-duality and non-geometric backgrounds
   Atish Dabholkar and Chris Hull
- AdS spacetimes from wrapped D3-branes
   Jerome P Gauntlett and Oisín A P Mac
   Conamhna



Nucl. Fusion 65 (2025) 016010 (16pp)

https://doi.org/10.1088/1741-4326/ad8fbc

# Fully-relativistic electron Bernstein wave current drive simulations in the STEP spherical tokamak

Bodhi Biswas<sup>1,\*</sup>, Simon Freethy<sup>2</sup> and Roddy Vann<sup>1</sup>

E-mail: bodhi.biswas@york.ac.uk

Received 11 June 2024, revised 27 October 2024 Accepted for publication 7 November 2024 Published 15 November 2024



#### **Abstract**

Electron Bernstein waves (EBWs) are theorised to efficiently drive current in spherical tokamak power plants, e.g. Spherical Tokamak for Energy Production (STEP). At high temperatures  $(T_e \gtrsim 4 \text{ keV})$ , relativistic effects can significantly impact wave propagation. This work presents relativistic calculations of EBW wave propagation, damping, and current drive (CD) in a conceptual STEP plasma. Kramers-Kronig relations are exploited to efficiently evaluate the fully-relativistic dispersion relation for arbitrary wave-vectors, leading to a  $> 50 \times$  speed-up compared to previous efforts. CD efficiency is calculated using both linear and quasilinear codes. Thus, for the first time, large parametric scans of fully-relativistic EBW CD simulations are performed through ray-tracing. In STEP, three main classes of rays are identified. The first class propagate deep into the core ( $\rho < 0.5$ ), but exist only if relativistic effects are accounted for. They damp strongly at the fundamental harmonic on nearly-thermal electrons and thus drive little current. A second class of rays propagate to intermediate depths ( $\rho \approx 0.3 - 0.7$ ) before damping at the 2nd harmonic. Their CD efficiencies are significantly altered due to relativistic changes to trajectory and polarisation. The third class of rays damp strongly far off-axis  $(\rho > 0.7)$ , predominantly at the second harmonic. These ray trajectories are sufficiently short and 'cold' that relativistic effects are unimportant. In linear CD simulations, the optimal launch point corresponds to this third class of rays, suggesting that non-relativistic simulations are adequate. However, quasilinear calculations indicate that, at reactor relevant powers, CD is maximised at  $\rho \approx 0.6$ . This quasilinear optimal point corresponds to the second class of rays, for which relativistic propagation does matter.

Keywords: EBW, STEP, EBCD

(Some figures may appear in colour only in the online journal)

© BY

Original Content from this work may be used under the terms of the Creative Commons Attribution 4.0 licence. Any

further distribution of this work must maintain attribution to the author(s) and the title of the work, journal citation and DOI.

York Plasma Institute, School of Physics, Engineering & Technology, University of York, York, United Kingdom of Great Britain and Northern Ireland

<sup>&</sup>lt;sup>2</sup> UKAEA, Culham Campus, Abingdon, United Kingdom of Great Britain and Northern Ireland

<sup>\*</sup> Author to whom any correspondence should be addressed.

#### 1. Introduction

Electron Bernstein waves (EBWs) can drive toroidal current in tokamaks by asymmetrically damping on a resonant electron population. EBWs do not have a density cutoff, making them attractive as a current drive (CD) actuator in overdense plasmas ( $\omega_{\rm pe} > \Omega_{\rm e}$ , where  $\omega_{\rm pe}$  and  $\Omega_{\rm e}$  are the electron plasma and electron cyclotron frequency, respectively) [1]. For example, off-axis (OA) EBW current drive (EBCD) is expected to be three times as efficient as electron cyclotron CD during steady-state operation in STEP [2–4]. It is therefore being strongly considered as a current-drive actuator for STEP, where >100 MW of microwave power (delivered by hundreds of 1 MW class gyrotrons) will be used to deliver  $\sim$  4 MA of auxiliary steady-state current. The resulting current-drive system requires significant recirculating power. Its efficiency is a critical factor in optimising  $Q_{\rm eng}$ .

EBCD performance can be sensitive to plasma and launch conditions, and so accurate modelling of wave propagation, damping, and electron response is necessary. Propagation is typically modelled using ray-tracing, while Fokker–Planck codes model damping and the electron response [5, 6]. Relativistic effects can significantly impact wave *damping* and the *electron current response*. Relativistic fast electrons shift and broaden the cyclotron resonance, and it is standard practice to model these effects. A relativistic population also impacts CD efficiency through the modification of collisionality, and is therefore routinely modelled in linear and quasilinear CD codes. In both cases, the direct, relativistic interaction between the EBW and the electrons is limited to the cyclotron resonance curve in momentum-space.

Relativistic *propagation* may also be important at reactor-relevant temperatures. Modifications to the wave trajectory in  $(\mathbf{r}, \mathbf{k})$ -space and its polarisation will affect CD performance. In addition, relativistic effects cause a narrowing of the low-field-side cyclotron resonance [7]. In simulations that employ relativistic damping but non-relativistic ray trajectories, this narrowing can cause the weak-damping approximation to break (making ray-tracing invalid) prior to the complete depletion of ray power. This problem is frequently encountered in STEP simulations for rays that propagate sufficiently far into the core ( $\rho$  < 0.4) and approach the fundamental harmonic. To model this parameter regime, and to ensure accuracy elsewhere, requires simulating relativistic propagation.

This is challenging. Unlike the resonant damping, propagation requires evaluating the Hermitian contribution to the dielectric tensor. Doing so for the fully-relativistic, kinetic dispersion is numerically cumbersome. Trubnikov first derived the fully-relativistic dispersion by linearising the Vlasov equation and applying the method of unperturbed orbits [8]. Treating the time integral analytically produces a 2D velocity integral  $(v_{\perp}, v_{||})$  that must be evaluated numerically. This is Trubnikov's '1st Form'. The integrand quickly decays with |v|, but numerical challenges persist due to poles along resonance curves. Weiss developed a numeric technique for this integral [9], but it is still slow because it is 2D. Trubnikov's '2nd Form' treats the velocity integral analytically, leaving a

1D time integral that must be evaluated numerically. This is typically faster to evaluate than the 1st Form. However, the integrand is highly oscillatory in time and roughly decays as  $\exp\left(-|N_{\parallel}|t\right)$ , where  $N_{\parallel}$  is the parallel refractive index. In a toroidal geometry,  $N_{\parallel}$  is not conserved and can become arbitrarily small, leading to significant slowing down of the ray-tracer. Previous efforts to simulate relativistic EBW propagation and damping use approximate slab-geometries such that the ray-tracing equations are not needed [7, 10]. One notable exception is ray-tracing studies in ARIES-ST by Nelson-Melby  $et\ al\ [11]$ . They report that each ray simulation requires several wall-clock hours (as opposed to several seconds for a non-relativistic ray). Such numerical expense has made difficult a thorough investigation of the effects of relativistic propagation on CD.

Numerous efforts have been made at approximating the fully-relativistic dispersion [12–16]. These are commonly referred to as 'weakly-' or 'moderately-'relativistic treatments since they take the limit  $\mu_{\rm e} \equiv c^2/v_{\rm te}^2 \gg 1$ , where c is the speed of light and  $v_{\rm te} = \sqrt{T_{\rm e}/m_{\rm e}}$  is the thermal electron velocity. These formulations are often also constrained to small  $N_{||}$  and either the small or large  $\lambda$  limit (where  $\lambda = \mu_{\rm e}^{-1}(N_{\perp}/Y)^2$  is the Larmor-radius parameter and  $Y \equiv \Omega_{\rm e}/\omega$ ). A helpful review of various weakly relativistic dispersions can be found in Volpe et~al~ and references therein [16]. Constraints on Larmor radius are particularly limiting for EBWs, as  $\lambda$  can span from  $\ll 1$  prior to X-B mode-conversion, to  $\gtrsim 1$  afterwards. Constraints on  $\lambda$  aside, the validity of weakly-relativistic models is questionable for reactor-relevant temperatures ( $T_{\rm e} \sim 20~{\rm keV}$  or equivalently  $\mu_{\rm e}^{-1} \sim 0.04$ ).

This work applies a fully-relativistic kinetic dispersion to the problem of O-X-B launch, both in a slab and toroidal geometry. (Here, 'O', 'X', and 'B' denote the cold ordinary and extra-ordinary modes, and the EBW, respectively.) Following Pavlov and Castejon [17], the Kramers–Kronig relations are exploited to efficiently evaluate the Hermitian part of the fully-relativistic dielectric tensor. (It is relatively easy to evaluate the anti-Hermitian part of the fully-relativistic dielectric tensor.) At low  $N_{||}$ , the result is a numeric scheme that is  $\sim 100x$  faster than direct evaluation of Trubnikov's 2nd form. Its accuracy is exact, and its efficiency is independent of  $N_{||}$ . (Consequently, it is also applicable to the study of direct X-B launch at low  $N_{||}$ .)

A ray-tracer is developed to solve fully-relativistic EBW trajectories in a toroidal geometry. It is coupled to a linear adjoint model [18] to provide quick estimates of CD at low microwave power. The ray-tracer is also coupled to CQL3D [19] to account for quasilinear effects at high powers. In doing so, the impact of relativistic propagation on CD efficiency is modelled for the first time. This modelling workflow is applied to a conceptual STEP plasma to demonstrate important relativistic effects that are presently neglected in non-relativistic simulations. We highlight a particular class of relativistic rays that propagate deep into the STEP plasma ( $\rho$  < 0.5) and strongly damp at the fundamental harmonic. These rays cannot be modelled with a non-relativistic dispersion without the weak-damping approximation breaking.

Section 2 formulates the numeric scheme for evaluating the fully-relativistic dispersion using Kramers–Kronig relations. Section 3 tests this dispersion against others by evolving the ray-tracing equations in a slab geometry. Section 4 applies this model to a toroidal ray-tracer with STEP plasma parameters. The impact of relativistic effects on CD efficiency is discussed, both in the linear (low-power) and quasilinear (high-power) regime. Section 5 summarises these findings, and conclude that relativistic propagation is indeed important to model in STEP.

# 2. Fast evaluation of relativistic dispersion

We seek to construct a fast, numerically robust method to evaluate the fully-relativistic EBW dispersion relation. We start with Trubnikov's 1st Form [8, 20]. It is assumed that the wave frequency is much larger than the ion cyclotron and ion plasma frequencies ( $\omega \gg \Omega_i, \omega_{pi}$ ) and so ion dynamics can be ignored. The susceptibility tensor in Stix coordinates [21] is

$$\chi_{ij} = \sum_{n = -\infty}^{\infty} \chi_{ij}^n \tag{1a}$$

$$\chi_{ij}^{n} = -\frac{X}{2} \frac{\mu_e^2}{K_2(\mu_e)} F_{ij}^{n} \tag{1b}$$

$$F_{ij}^{n} = \int_{-\infty}^{\infty} \mathrm{d}\bar{p}_{\parallel} \int_{0}^{\infty} \mathrm{d}\bar{p}_{\perp}\bar{p}_{\perp} \frac{e^{-\mu_{\rm e}\gamma_{\rm e}}}{\gamma_{\rm e}} \frac{P_{ij}^{n}}{\gamma_{\rm e} - N_{\parallel}\bar{p}_{\parallel} - nY} \qquad (1c)$$

where  $X \equiv \omega_{\rm pe}^2/\omega^2$ ,  $K_2$  is the MacDonald function of 2nd type,  $\bar{p} \equiv p/(m_{\rm e}c)$  is normalised particle momentum,  $\gamma_{\rm e} = \sqrt{1+\bar{p}^2}$  is the Lorentz factor, and n is the cyclotron harmonic. The subscripts '||' and ' $\perp$ ' denote the parallel and perpendicular component with respect to the background magnetic field. The dyadic elements  $P_{ij}^n$  are functions of  $\bar{p}_{\parallel}$ ,  $\bar{p}_{\perp}$ ,  $\nu_{\parallel}$ , and  $\nu_{\perp}$ , where  $\nu \equiv N/Y$ . These elements are

$$P_{11}^n = \frac{n^2}{\nu_\perp^2} J_n^2 \tag{2a}$$

$$P_{12}^{n} = -P_{21}^{n} = \frac{i\bar{p}_{\perp}n}{\nu_{\perp}} J_{n}J_{n}'$$
 (2b)

$$P_{13}^{n} = P_{31}^{n} = -\frac{\bar{p}_{\parallel}n}{\nu_{\perp}}J_{n}^{2}$$
 (2c)

$$P_{22}^n = \bar{p}_{\perp}^2 J_n^{\prime 2} \tag{2d}$$

$$P_{23}^n = -P_{32}^n = i\bar{p}_{\parallel}\bar{p}_{\perp}J_nJ_n'$$
 (2e)

$$P_{33}^n = \bar{p}_{||}^2 J_n^2 \tag{2f}$$

where  $J_n = J_n(\nu_\perp \bar{p}_\perp)$  is the Bessel function of the 1st kind, and  $J'_n$  is its first derivative.

The variable change  $\bar{p}_{\perp} \rightarrow \gamma_{\rm e}$  is taken, resulting in

$$F_{ij}^{n} = \int_{-\infty}^{\infty} \mathrm{d}\bar{p}_{\parallel} I_{ij}^{n} \left(\bar{p}_{\parallel}\right) \tag{3a}$$

$$I_{ij}^{n}\left(\bar{p}_{\parallel}\right) = \int_{1}^{\infty} \mathrm{d}\gamma_{\mathrm{e}} \mathrm{e}^{-\mu_{\mathrm{e}}\gamma_{\mathrm{e}}} \frac{P_{ij}^{n}}{\gamma_{\mathrm{e}} - N_{\parallel}\bar{p}_{\parallel} - nY}.\tag{3b}$$

The integrand in equation (3b) has a pole at

$$\gamma_{\rm e} = N_{\parallel} \bar{p}_{\parallel} + nY \equiv \gamma_{\rm e}^n. \tag{4}$$

This pole represents the wave-particle resonance, and therefore contributes to the anti-Hermitian (AH) component of the susceptibility  $\chi$ . We rewrite:

$$I_{ij}^{n}\left(\bar{p}_{\parallel}\right) = I_{ij}^{n,H} + iI_{ij}^{n,AH} \tag{5a}$$

$$I_{ij}^{n,H} = \mathcal{P} \int_{1}^{\infty} d\gamma_{e} e^{-\mu_{e}\gamma_{e}} \frac{P_{ij}^{n}}{\gamma_{e} - \gamma_{e}^{n}}$$
 (5b)

$$I_{ii}^{n,AH} = \pm \pi e^{-\mu_e \gamma_e^n} P_{ii}^n \left( \bar{p}_{\perp} \left( \bar{p}_{\parallel}, \gamma_e^n \right) \right) \tag{5c}$$

where H denotes the Hermitian part, and  $\mathcal{P}$  denotes the principal value. In equation (5c),  $\bar{p}_{\perp}$  is evaluated at the pole and is therefore a function of  $\bar{p}_{\parallel}$  and  $\gamma_{\rm e}^n$ , in accordance with equation (4). The Sokhotski-Plemelj theorem has been used. The ambiguity regarding the  $\pm$ -sign in equation (5c) is resolved by following the Landau prescription. Expanding around the pole in  $\omega_i$  reveals  $\gamma_{\rm e}^n \approx (ck_{\parallel}\bar{p}_{\parallel} + n\Omega_{\rm e})(\omega_r - i\omega_i)/\omega_r^2$ . Next, for a wave with positive real frequency,  $ck_{\parallel}\bar{p}_{\parallel} + n\Omega_{\rm e} > 0$  must hold for the wave-particle resonance to exist. With these two considerations, it follows that the pole must be kept *below* the integration contour in complex  $\gamma_{\rm e}$ -space. Accordingly, the minus-sign should be used.

The AH component of  $F_{ii}^n$  is simply

$$F_{ij}^{n,AH} = -\pi \int_{-\infty}^{\infty} d\bar{p}_{\parallel} e^{-\mu_{e} \gamma_{e}^{n}} P_{ij}^{n} \left( \bar{p}_{\perp} \left( \bar{p}_{\parallel}, \gamma_{e}^{n} \right) \right)$$
 (6)

Equation (6) is a 1D integral along the resonance curve in momentum-space. The integration domain is bounded for  $|N_{\parallel}| < 1$ . Even for  $|N_{\parallel}| \geqslant 1$ , the integrand quickly decays as  $\gamma_e^n$  grows. Substitution into equation (1b) then provides

$$\chi_{ij}^{n,AH} = -\frac{X}{2} \frac{\mu_{\rm e}^2}{K_2(\mu_{\rm e})} F_{ij}^{n,AH} \tag{7}$$

Kramers–Kronig (KK) relations [22, 23] can be exploited to quickly evaluate  $\chi_{ij}^{n,H}$ . Their application to linear plasma waves is reported in Brambilla's textbook [24]. Pavlov and Castejon [17] have recently applied such a strategy to evaluating the fully-relativistic EBW dispersion relation. This paper applies a slightly different formulation which is quantitatively identical.

Suppose one wishes to evaluate  $\mathcal{F}(\omega, \mathbf{k}) = \mathcal{G}(\omega, \mathbf{k}) + i \mathcal{Q}(\omega, \mathbf{k})$ , where  $\mathcal{G}$  and  $\mathcal{Q}$  are real. Assume  $\mathcal{F}$  is analytic in

the upper-half plane in complex  $\omega$ -space and decays such that  $\lim_{\omega \to \pm \infty} |\mathcal{F}| \to 0$ . Then the following KK relations apply:

$$\mathcal{G}(\omega, \mathbf{k}) = \frac{1}{\pi} \mathcal{P} \int_{-\infty}^{+\infty} \frac{\mathcal{Q}(\omega', \mathbf{k})}{\omega' - \omega} d\omega'$$
 (8a)

$$Q(\omega, \mathbf{k}) = -\frac{1}{\pi} \mathcal{P} \int_{-\infty}^{+\infty} \frac{\mathcal{G}(\omega', \mathbf{k})}{\omega' - \omega} d\omega'. \tag{8b}$$

We limit the integration to positive  $\omega$  by taking equations (8) and multiplying the numerator and denominator by  $(\omega' + \omega)$ . This results in

$$\mathcal{G}(\omega, \mathbf{k}) = \begin{cases} \frac{2}{\pi} \mathcal{P} \int_{0}^{+\infty} \frac{\omega' \mathcal{Q}(\omega', \mathbf{k})}{\omega'^{2} - \omega^{2}} d\omega' & \text{if } \mathcal{Q}(\omega) \text{ is even.} \\ \frac{2\omega}{\pi} \mathcal{P} \int_{0}^{+\infty} \frac{\mathcal{Q}(\omega', \mathbf{k})}{\omega'^{2} - \omega^{2}} d\omega' & \text{if } \mathcal{Q}(\omega) \text{ is odd.} \end{cases}$$

and a similar relation for  $\mathcal{Q}(\omega,\mathbf{k})$ . Thus, equations (9) can be used to evaluate

$$\chi_{ij}^{n,H}(\omega,\mathbf{k}) = \begin{cases} \frac{2}{\pi} \mathcal{P} \int_{0}^{+\infty} \frac{\omega' \chi_{ij}^{n,AH}(\omega',\mathbf{k})}{\omega'^{2} - \omega^{2}} d\omega' & (i,j) = (1,1), (1,3), (2,2), (3,3) \\ \frac{2\omega}{\pi} \mathcal{P} \int_{0}^{+\infty} \frac{\chi_{ij}^{n,AH}(\omega',\mathbf{k})}{\omega'^{2} - \omega^{2}} d\omega' & (i,j) = (1,2), (2,3). \end{cases}$$

$$(10)$$

Note that  $\chi_{ij}^{n,H}$  and  $\chi_{ij}^{n,AH}$  are not restricted to purely real functions. This can be shown by separating  $\chi_{ij}^{n,H}$ ,  $\chi_{ij}^{n,AH}$  into real and imaginary parts and applying the KK relations to each. Evaluating  $\chi_{ij}^{n,H}$  requires a single 1D integration along  $\omega'$  in the 'outer loop', and 1D integrations along  $\gamma_e$  in the 'inner loop' to evaluate  $\chi_{ij}^{n,AH}(\omega')$  (see equations (6) and (7)). The integration domain of the outer loop can be further bounded by realising that the resonance curve exists only for  $n^2Y^2+N_{||}^2>1$ . Accordingly, the upper-bound of the integration in equation (10) is truncated to  $\omega'<\Omega_e\sqrt{n^2+N_{||}^2/Y^2}$ . In this domain, the integrand is smooth, allowing for an efficient Gaussian-quadrature scheme. The singularity at  $\omega'=\omega$  is handled using techniques similar to those described in section 3 of Weiss [9].

Through the KK relations,  $\chi_{ij}^{n,H}$  is roughly proportional to  $\chi_{ij}^{n,AH}$ . Therefore, only the cyclotron harmonic minimising |1-nY|—and its neighbouring harmonics—will be nonnegligible. Correspondingly, only a few terms in the series are needed for convergence. More terms are needed in the presence of strong harmonic overlap (i.e. if  $T_{\rm e}$  and  $|N_{||}|$  are sufficiently large).

Figure 1 plots the speed at which the fully-relativistic dispersion is evaluated using the KK method. It is compared against an optimised evaluation of Trubnikov's 2nd formula using numeric techniques borrowed from the code R2D2 [7]. (A direct evaluation of Trubnikov's 1st formula, without the use of KK relations, is not plotted. It is much too slow.)

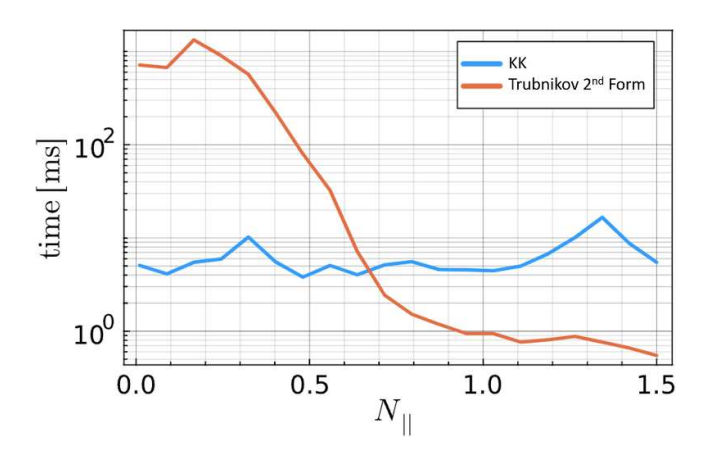


**Figure 1.** Benchmark of speed at which the fully-relativistic dispersion relation in numerically evaluated. A relative error tolerance of  $10^{-7}$  is used. Speed of evaluating Trubnikov's 2nd Form is strongly dependent on  $N_{\parallel}$ . Wave-parameters:  $N_{\perp}=5$ , X=1.3, Y=0.66,  $\mu_{\rm e}^{-1}=0.02$ . Test conducted with the *Julia* bench-marking tool *BenchmarkTools.jl* and using a AMD Ryzen 7 3700X 4.05 GHz CPU.

Trubnikov's 2nd form is faster at high  $N_{||}$ . However, as  $N_{||}$  drops, the dispersion relation becomes increasingly slow to converge. This can be particularly problematic in toroidal geometries, where  $N_{||}$  along a ray is not conserved and can become small. In some cases, a single ray trajectory can take several hours as it approaches very small  $N_{||}$ . In contrast, the speed of convergence for the KK-formula is independent of  $N_{||}$ , making it clearly favourable in situations where  $N_{||} \lesssim 0.65$ . (This  $N_{||}$ , at which both methods perform equally well, is weakly sensitive to other wave parameters.) In toroidal geometry (see section 4), an optimised ray-tracing scheme will be employed to switch between the two dispersions depending on  $N_{||}$ .

#### 3. Relativisitic effects in slab geometry

Calculation of the fully relativistic dispersion using the KK relations is verified in a ray-tracing simulation of O-X-B launch in slab geometry. Details of the ray-tracer can be found in appendix A. The magnetic field is directed along the z-direction, while density varies in the x-direction. A hyperbolic tangent function is used for the density profile, as shown in figure 2. The density gradient at the cutoff is set to  $k_0L_n = 10$ , with  $k_0$  being the vacuum wave-number and  $L_n \equiv n_e/|\partial_x n_e|$  being the density scale-length.

An O-mode is launched into the high-density region at the optimal angle for O-X mode-conversion  $(N_{||} \equiv N_z = \sqrt{Y/(1+Y)})$ . In these runs, the magnetic field is uniform and Y=0.77 everywhere. Electron temperature is 1 keV. Figure 3 shows the ray trajectory in real-space (left) and phase-space (right) as a function of x. Three dispersion relations are plotted: (1) the non-relativistic, warm dispersion, (2) the fully-relativistic KK formula, and (3) the fully-relativistic Trubnikov 2nd form. The latter two should be quantitatively identical, which enables the benchmarking of our code.

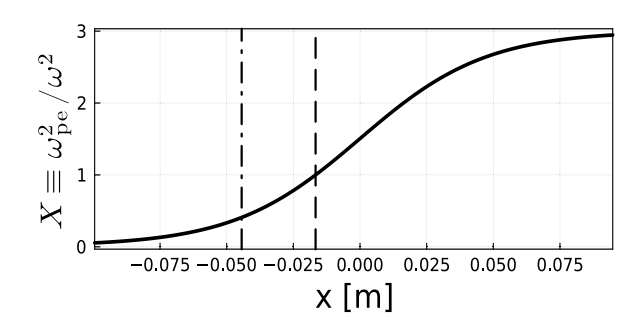


**Figure 2.** Density profile in slab geometry. Dashed vertical line denotes O-mode density cutoff (X = 1). Dash-dotted vertical line denotes the upper hybrid resonance (UHR), which corresponds to  $X + Y^2 = 1$ .

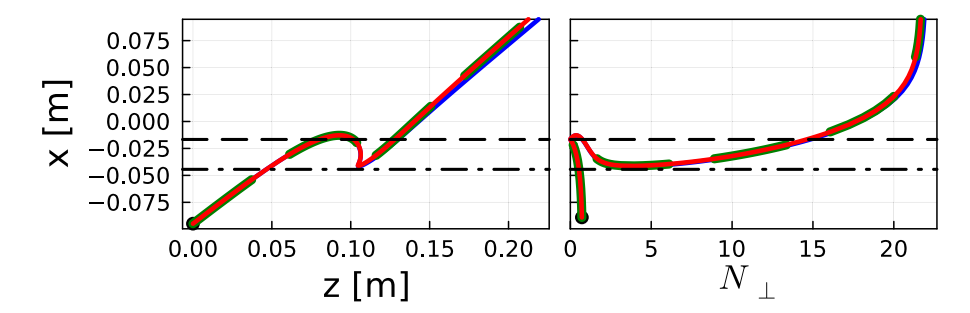
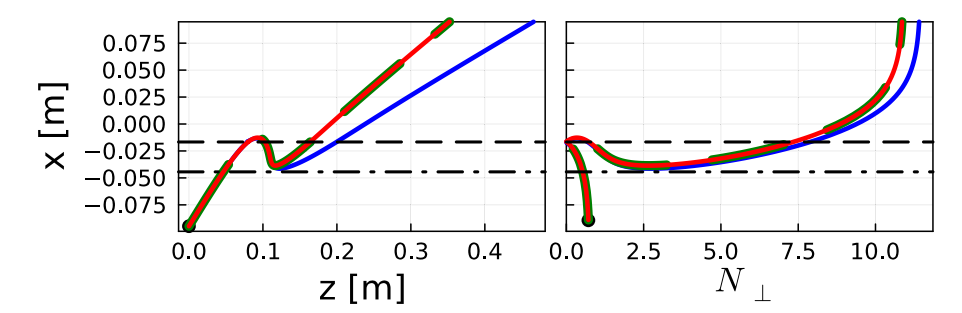


Figure 3. Ray trajectories in slab geometry (see figure 2) with  $T_e = 1$  keV. Blue: non-relativistic. Red: KK. Green dashed: Trubnikov 2nd Form. Dashed line denotes the O-Mode cutoff. Dash-dotted line denotes the UHR.



**Figure 4.** Ray trajectories in slab geometry (see figure 2) with  $T_e = 4 \text{ keV}$ . Blue: non-relativistic. Red: KK. Green dashed: Trubnikov 2nd Form. Dashed line denotes the O-Mode cutoff. Dash-dotted line denotes the UHR.

The three dispersions show excellent agreement until the X-mode begins converting to the EBW, at which point the non-relativistic dispersion slightly over-estimates  $N_{\perp}$ . In addition, the non-relativistic ray travels slightly more obliquely (in the z direction). These results indicate a slight disagreement between the non-relativistic and relativistic Bernstein modes.

Figure 4 repeats the previous exercise at  $T_e = 4\,\mathrm{keV}$ . The disagreement in ray trajectories following the X-B mode-conversion is now significantly larger. Note that STEP operates with a pedestal temperature of  $\sim 4\,\mathrm{keV}$ , which coincides with the UHR. This suggests that relativistic propagation may significantly impact EBCD.

This exercise is repeated for  $T_{\rm e}=15\,{\rm keV}$ , which is more representative of core temperatures in a fusion power plant. Since ray-tracing is being employed, we must check that the weak-damping condition remains valid along the trajectory ( $|{\rm Im}\,(N_\perp)|\ll R\,(N_\perp)$ ). This requires keeping  $T_{\rm e}\approx 3\,{\rm keV}$ 

near the UHR, and then ramping up  $T_e$  sufficiently far away from this region. One such temperature profile is shown in figure 5. The resulting dispersion relation and ray trajectories are shown in figure 6. The non-relativistic ray strongly diverges in both real and phase-space at  $T_{\rm e} \gtrsim 10\,{\rm keV}$ . The reason for this disagreement can be gleaned from plotting  $|\operatorname{Im}(N_{\perp})|/R(N_{\perp})$  along the rays. As  $T_{\rm e}$  increases, the nonrelativistic ray strongly damps at the Doppler-broadened 1st harmonic. The ratio  $\text{Im}(N_{\perp})/R(N_{\perp}) \approx 0.15$  (see figure 7). The weak-damping condition is violated, and the ray trajectory is no longer physical. If Y is increased (or equivalently, if  $\omega/\Omega_{\rm e}$ is decreased) such that the ray trajectory moves closer to the 1st harmonic resonance, this problem becomes more severe. Figure 8 demonstrates how the non-relativistic ray can acquire a group velocity faster than light for Y > 0.82 (equivalently,  $\omega/\Omega_{\rm e}$  < 1.22). In contrast, with relativistic effects included, the 1st harmonic resonance is weakened. The relativistic ray

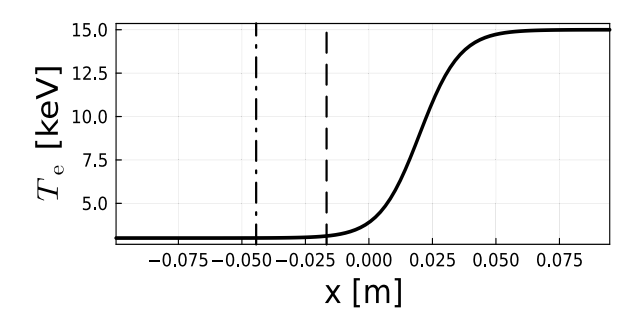


**Figure 5.** Modified slab geometry with tapered  $T_e$  profile. Solid vertical line denotes O-mode density cutoff. Dash-dotted vertical line denotes the UHR.

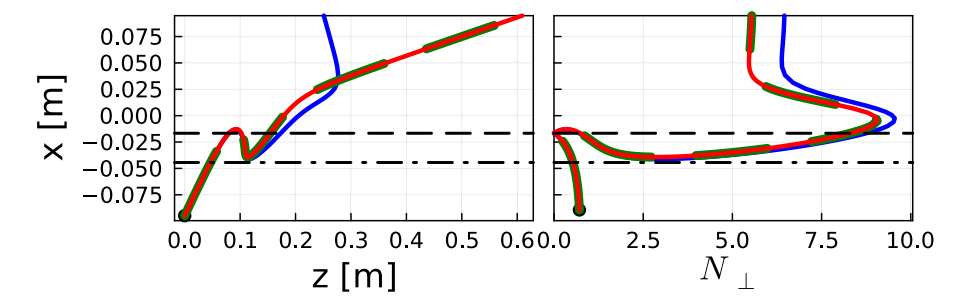


**Figure 6.** Ray trajectories in modified slab geometry (see figures 2 and 5). Blue: non-relativistic. Red: KK. Green dashed: Trubnikov 2nd Form. Dashed line denotes the O-Mode cutoff. Dash-dotted line denotes the UHR.

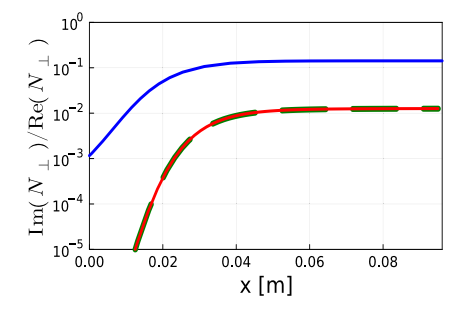


**Figure 7.** Imaginary perpendicular refractive index, normalised to real component, along rays in a modified slab geometry (see figures 2 and 5). Blue: non-relativistic. Red: KK. Green dashed: Trubnikov 2nd Form.

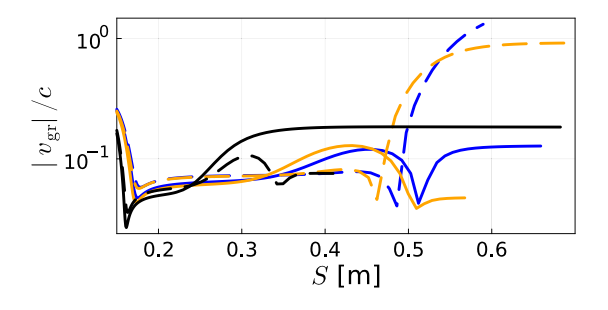


**Figure 8.** Group velocity versus distance along the ray trajectory (S) for  $\omega/\Omega_e=1.21$  (blue), 1.22 (orange), and 1.3 (black). Solid and dashed lines denote relativistic and non-relativistic rays, respectively. Using the modified slab geometry (see figures 2 and 5).

can therefore penetrate further into the plasma without breaking the weak-damping approximation. As will be shown in section 3, this effect can preclude ray-tracing simulations of

non-relativistic EBWs as they approach the low-field-side harmonic in STEP.

So far, the impact of relativistic effects on wave polarisation has not been commented on. Figure 9 plots the electric field components for the  $T_{\rm e}=15~{\rm keV}$  case. There is an small impact on  $E_{\parallel}$  and negligible impact on  $E_{-}$ . A study of this effect by Nelson-Melby et~al~[11] found this effect to be much larger. However, in that study, rays were evolved in a toroidal geometry and thus  $N_{\parallel}$  was not kept constant. This indicates that the direct impact of relativistic effects on wave polarisation is small. The indirect impact, via a modified phase-space trajectory, can be much larger.

It should also be noted that the choice of dispersion shifts the O-mode cutoff density away from  $\omega = \omega_{\rm pe}$ . This effect grows with  $T_{\rm e}$ . The new cutoff can be approximated by evaluating  $\omega = \omega_{\rm pe}$  with a relativistic mass correction  $m_{\rm e} \to \gamma m_{\rm e}$ , where  $\gamma$  is evaluated at  $v_{\rm te} = \sqrt{T_{\rm e}/m_{\rm e}}$ . For the temperatures under consideration, these shifts are at sub-millimetre scales. For example, they are only perceptible in the slab ray trajectories plotted in this section if zoomed in at the cutoff. This should have negligible impact on O-X mode-conversion in STEP.

# 4. EBCD modelling in STEP geometry

EBW CD performance—between the 1st and 2nd cyclotron harmonics—is scoped for a conceptual STEP operation point. (Note that this plasma is different from the one modelled in our earlier analysis [18].) It is similar to the EBCD+ECCD 'conservative confinement' steady-state operating point (a.k.a. EB-CC) detailed in Tholerus *et al* [4] With a bootstrap fraction of  $\sim 81\%$ , roughly 4 MA must be driven externally. (Please

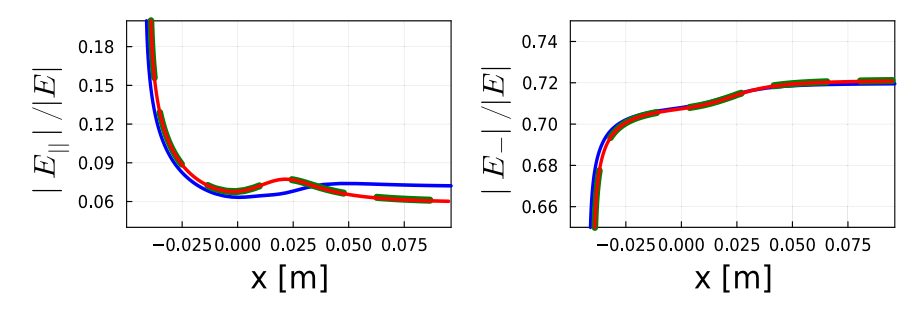


**Figure 9.** Wave polarisation along rays in a modified slab geometry (see figures 2 and 5). The component  $E_{\parallel} = E_z$  and  $E_{-}$  is the right-hand polarisation. Blue: non-relativistic. Red: KK. Green dashed: Trubnikov 2nd Form.

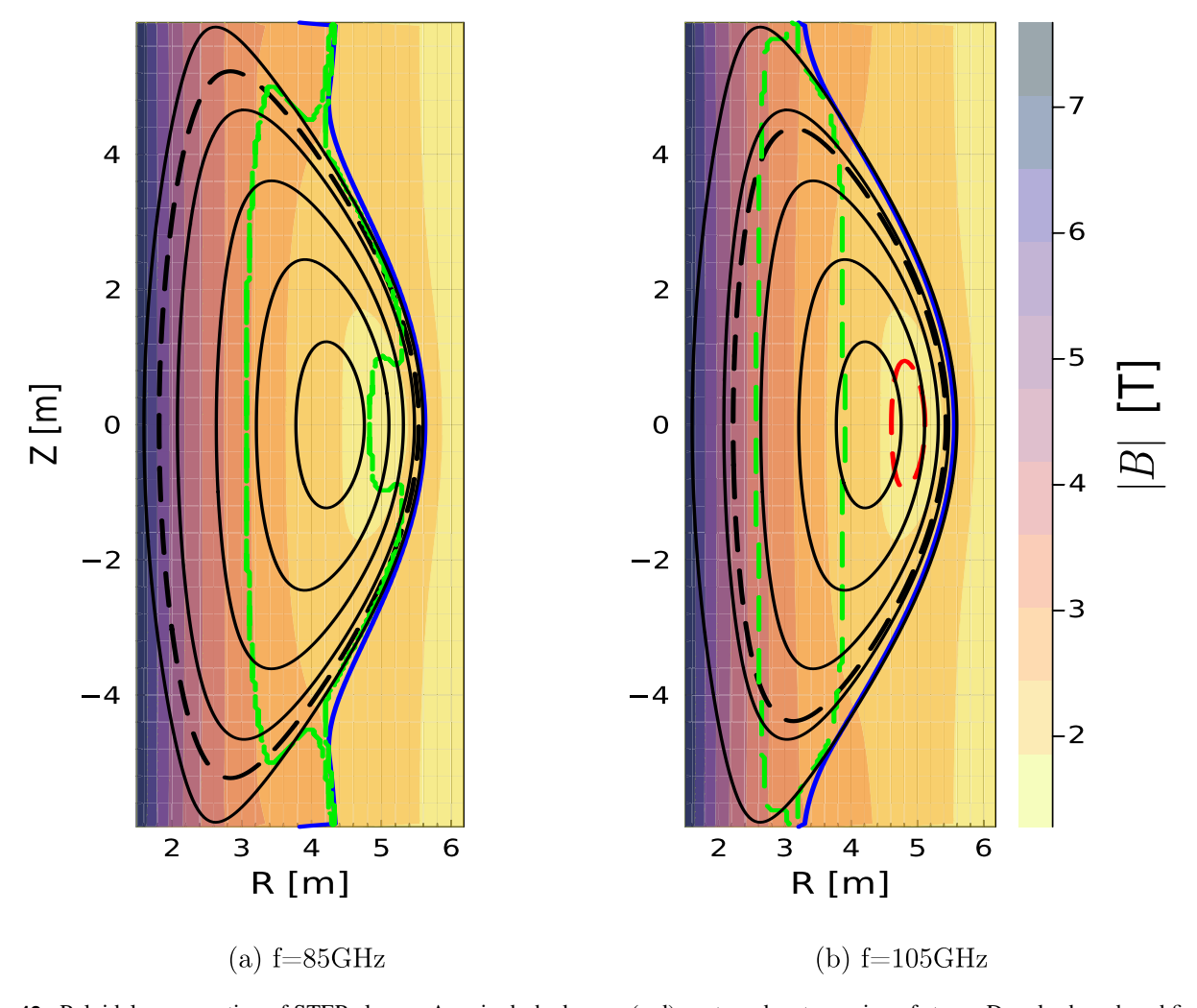
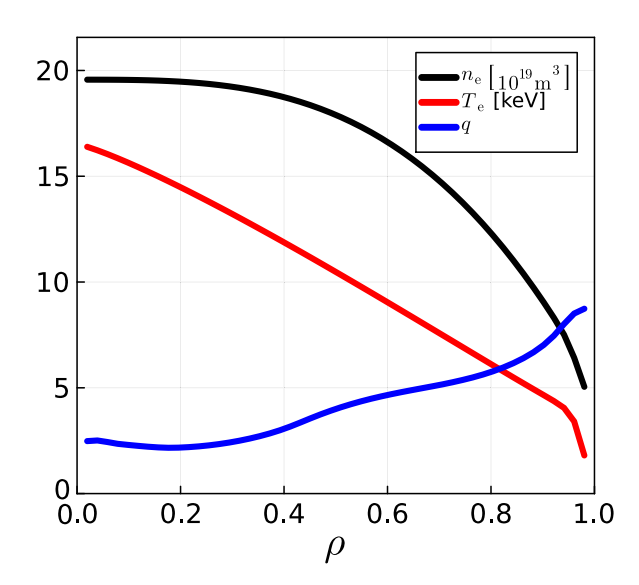


Figure 10. Poloidal cross-section of STEP plasma. Area in dashed green (red) contour denotes region of strong Doppler-broadened first (second) harmonic resonance, as determined by  $\omega = n\Omega_e \pm 3v_{\text{Te}}k_{\parallel}$  for  $N_{\parallel} = 0.5$ . Resonance contours correspond to microwave frequencies of 85 GHz (left) and 105 GHz (right). Black dashed contour denotes O-mode cutoff. Solid blue line denotes UHR. Solid black contours denote flux surfaces in increments of  $0.2\rho$ . Colourbar shows contours of total magnetic field. Toroidal magnetic field and plasma current are oriented counter-clockwise when viewed top-down.

refer to table 5 and figure 16 in [4] for the target CD requirements.) figures 10 and 11 summarise the parameters and geometry of this plasma. A  $Z_{\rm eff}$  of 2.5 is assumed everywhere. For the assumed microwave frequencies, the 1st harmonic resonance occurs on the inboard side, but can be accessed at larger R due to Doppler broadening. Likewise, the Doppler

broadened 2nd harmonic can be accessed as the EBW passes through the magnetic well near the outer mid-plane (visible in figure 10(b)). The 2nd harmonic is easier to access at higher microwave frequencies.

We have conducted a ray-tracing scan over launch parameters to find the optimal point(s) that maximise CD efficiency.



**Figure 11.** Radial equilibrium profiles in the plasma, where  $\rho \propto \sqrt{\psi_{\mathrm{tor}}}$ .

In the case of optimal O-X-B mode conversion, the wave  $|N_{||}$  at the O-mode cutoff ( $\omega = \omega_{pe}$ ) is already constrained: it should approach  $N_{\parallel,\text{opt}} = \sqrt{Y/(1+Y)}$  [1]. This constraint results in two free parameters for the microwave ray trajectory: frequency and poloidal launch height. We limit ourselves to considering microwave launch between 85 and 105 GHz. As seen in figure 10, frequencies above 105 GHz will move the O-mode cutoff well into the plasma, past the pedestal, where a high  $L_n$  will degrade the O-X mode-conversion efficiency. Likewise, frequencies below 90 GHz will move the upper-hybrid frequency (UHR) into the SOL, especially farther from the mid-plane. This should be avoided, given uncertainties in the SOL profile and the possibility of parasitic edge losses (i.e. collisional damping and parametric decay [25, 26]). For the purposes of exploring relativistic effects, we have extended the scan down to 85 GHz to capture an interesting class of rays that damp near-axis, further discussed in section 4.1.

The poloidal launch height is scanned via prescribing  $Z_{\rm OX}$ , which is the Z coordinate (in  $R,\phi,Z$  cylindrical coordinates) where the O-X mode-conversion takes place at the O-mode cutoff. At this point,  $N_{||}$  is set to  $N_{||,\rm opt}$  and  $N_{\perp}$  is simply zero. From this location the X-mode is evolved forward in time; it will initially travel into the plasma, then travel out towards the UHR, before mode-converting to the EBW and propagating into the core. In contrast, the O-mode is evolved backwards in time to determine the position and orientation of the external launcher. In this way, optimal O-X-B launch is forced in the simulation. From figure 10, it is evident that the upper hybrid resonance can be significantly outside the last closed flux surface (LCFS) for values of  $Z_{\rm OX}$  far from the mid-plane. Thus, the scan is limited to values of  $Z_{\rm OX}$  in the range -3.2 and +3.2 m.

The 2D scan (f,  $Z_{OX}$ ) determines all ray trajectories of interest for outboard O-X-B launch. An adjoint model [18]

is used to provide a rough estimate for CD efficiency. It captures both Fisch-Boozer [27] and Ohkawa [28] current-drive mechanisms, the latter of which is expected to be dominant far OA. The adjoint model is expected to fail for experimentally-relevant power levels, at which point quasilinear effects will impact CD location and efficiency. The quasilinear power threshold in STEP is expected to be ~1 MW launched microwave power [18], far below what is required for fully non-inductive operation. Section 4.2 briefly discusses quasilinear effects in STEP.

Figure 12 plots relativistic ray trajectories at three separate frequencies. The rays terminate when they have damped 99.9% of their initial power. While most rays terminate far OA ( $\rho > 0.7$ ), some rays above the mid-plane can propagate as deep as  $\rho \approx 0.3$ . It should be noted that at each OX mode-conversion point, there are two optimal wave-vector orientations. They correspond to  $N_{\parallel} = \pm N_{\parallel, \text{opt}}$  where  $N_{\parallel, \text{opt}} = \sqrt{Y/(1+Y)} > 0$ . The scans shown use  $N_{\parallel} = +N_{\parallel, \text{opt}}$ . The STEP equilibrium is top-down symmetric with respect to the mid-plane (Z=0). As a result, a scan using  $N_{\parallel} = -N_{\parallel, \text{opt}}$  results in a variant of figure 12 where the rays are flipped along the mid-plane. They also travel in the opposite toroidal direction and therefore drive current in the reverse direction.

Figure 13 plots the radial location of peak power deposition and the total current driven—both as functions of f and  $Z_{\rm OX}$ . Rays are shown to most commonly damp far OA. The exception is a group of rays launched above the mid-plane. This can be attributed to an initial downshift of  $|N_{||}|$  following O-X mode-conversion, which narrows the Doppler broadened 2nd harmonic and therefore weakens strong resonant damping at the edge. In some cases, the ray may propagate far enough to damp near axis (NA) at the 1st harmonic. In contrast, rays launched below the mid-plane undergo an  $|N_{||}|$  upshift, leading to swift resonant damping at the edge. This is explored in more detail in section 4.1.

Current-drive is maximised for rays with  $f \approx 98\,\mathrm{GHz}$  and  $Z_{\mathrm{OX}} \approx -1\,\mathrm{m}$ . Figure 14 reveal that these below mid-plane launch parameters predominantly lead to strong damping on the 2nd harmonic, and therefore drive current predominantly through the Ohkawa mechanism. At lower frequencies, the damping mechanism smoothly transitions to far OA 1st harmonic damping, which can be either Ohkawa or Fisch-Boozer dominant. Concurrent 1st and 2nd harmonic damping is possible due to a large Doppler broadening of both resonances. It is found that OA 1st harmonic damping is not particularly attractive for this STEP operating point.

# 4.1. Importance of relativistic ray trajectories

It is worthwhile to inspect a few exemplar rays to better understand their phase-space evolution and other factors impacting CD location and efficiency. It would also be helpful to determine when relativistic propagation effects matter. Hence, the previous linear scan is repeated but with non-relativistic

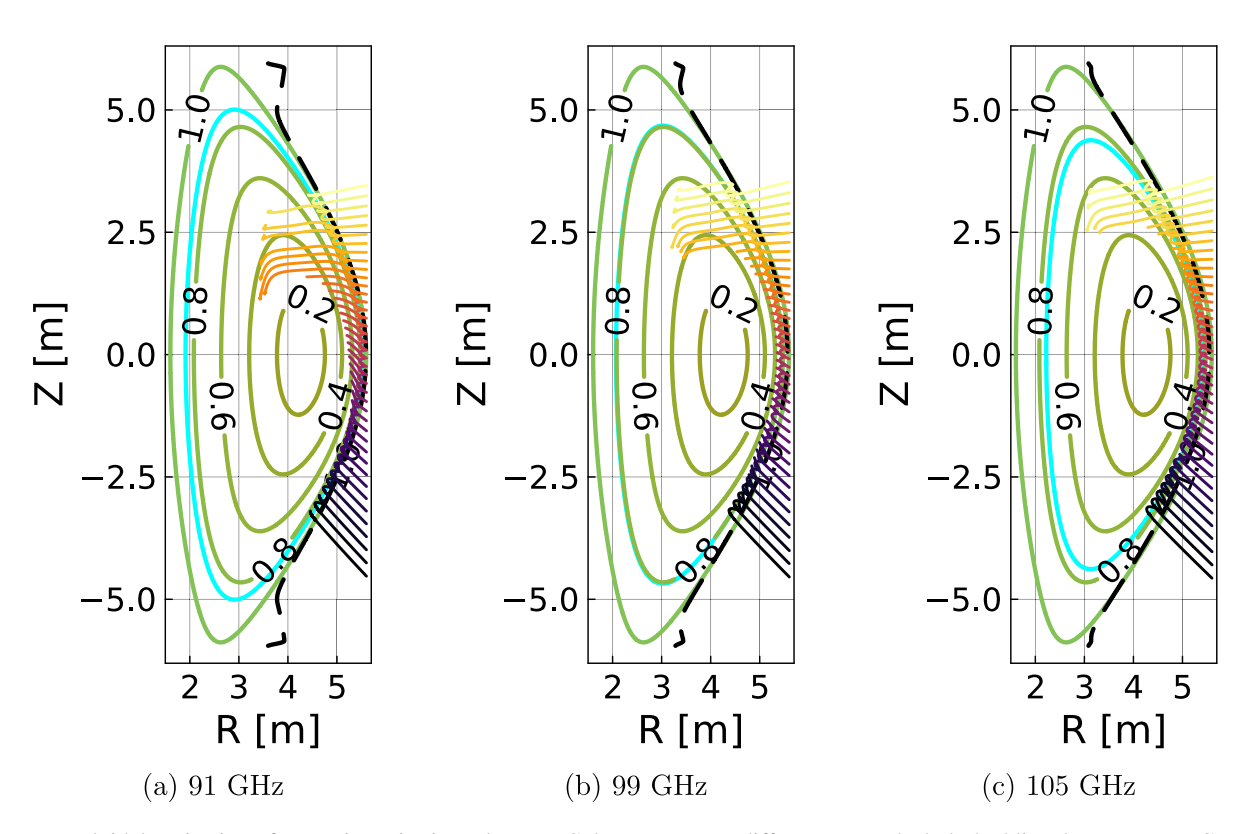
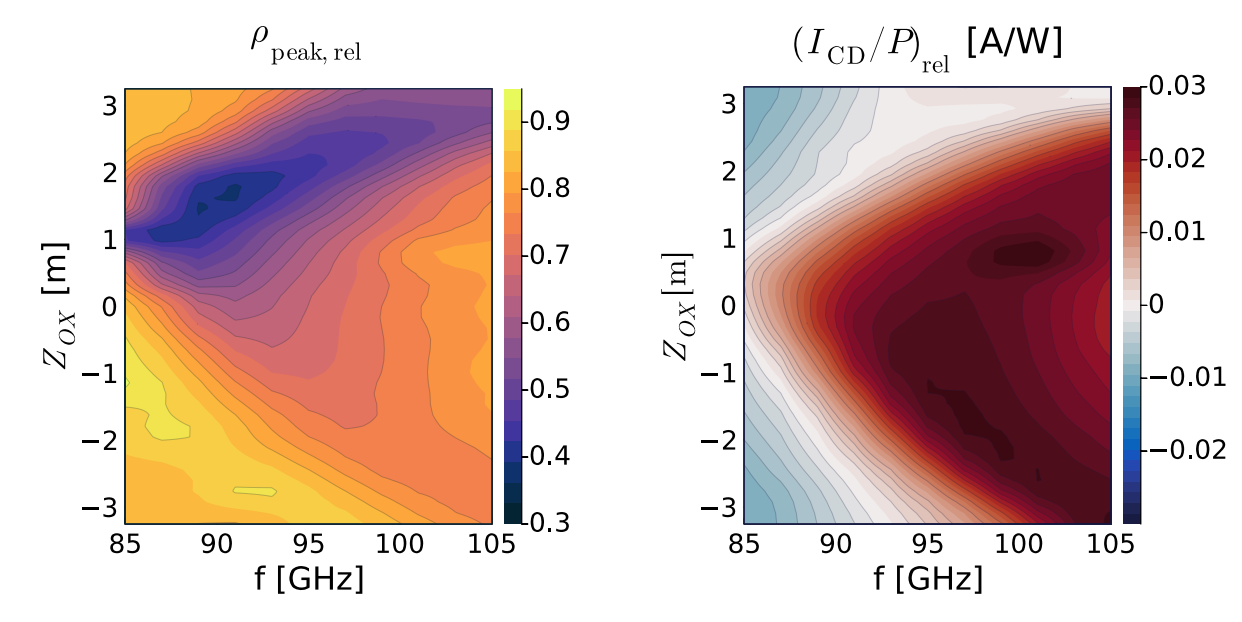


Figure 12. Poloidal projection of ray trajectories in real-space. Colours represent different  $Z_{OX}$ . Black dashed line denotes UHR. Cyan contour denotes the O-mode cutoff.



**Figure 13.** Left: radial location of peak power deposition. Right: total current driven assuming 1 MW of launched microwave power.  $I_{\text{CD}} > (<)0$  denotes co- (counter-) current drive.

ray trajectories. In the non-relativistic simulations, resonant damping is still calculated relativistically. For details, see appendix B. This 'mixed' approach is taken for two reasons. (1) Relativistic effects are known to strongly impact *damping*, even in present-day devices. Thus, this mixed approach is the standard method in existing EBW ray-tracers. (2) In comparing against the mixed approach, the impact of relativistic *propagation* is isolated.

These studies reveal three notable classes of rays.

**Near Axis (NA) rays:** the first class of rays are categorised as 'Near Axis' damping, or NA, rays. See figures 15 and 16 for examples of such rays at 87 GHz. These rays are launched above the mid-plane such that they initially undergo an  $|N_{||}|$  downshift following O-X mode-conversion. Eventually, they pass through  $N_{||} = 0$  at  $\rho < 0.4$ . Next,  $|N_{\perp}|$  increases as the

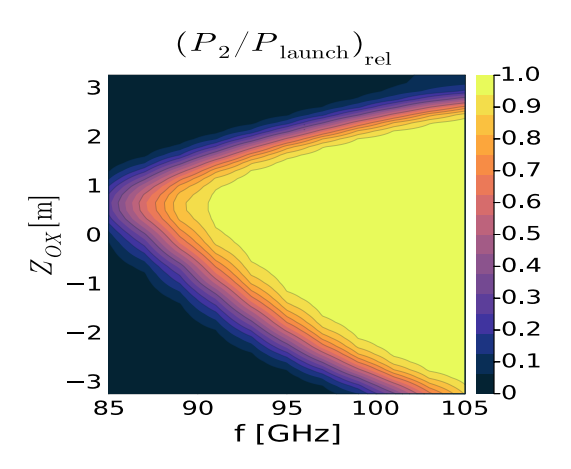
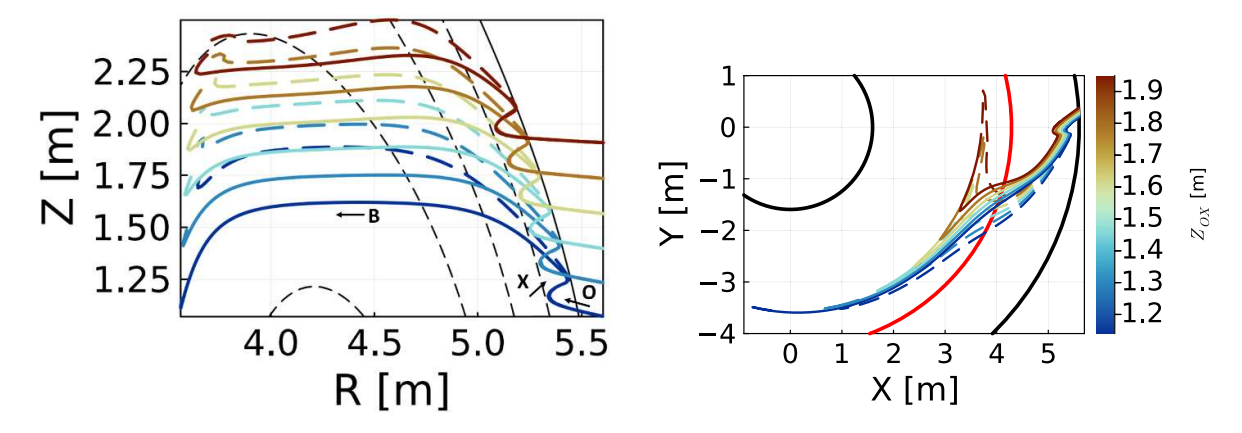


Figure 14. Fraction of launched power damped at the 2nd harmonic. Remaining power is damped at the 1st harmonic.



**Figure 15.** Near axis (NA) rays at 87 GHz. Poloidal (*a*) and top-down (*b*) projection of ray trajectories. Solid: relativistic. Dashed: non-relativistic. In (*a*), black dashed curves show flux surfaces and the black solid curve shows the LCFS. The propagation directions in the poloidal plane of O, X and B waves are indicated by arrows. In (*b*), the solid red curve indicates the magnetic axis and the solid black curves indicates where the LCFS intercepts the mid-plane.

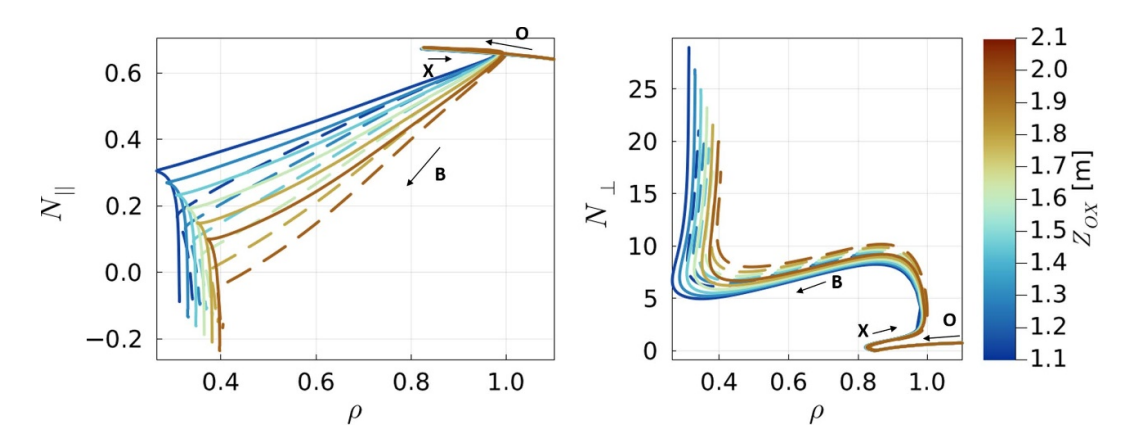


Figure 16. NA rays: ray trajectories in phase-space. Solid: relativistic. Dashed: non-relativistic

ray approaches the 1st harmonic. Sufficiently close to the 1st harmonic, the ray will strongly damp the remainder of its power.

Figures 15 and 16 reveal significant differences between the non-relativistic and relativistic ray trajectories, in both real and phase-space. The disagreements begin near the UHR, as expected from slab modelling, and continue to grow as the EBW propagates further into core.

Of particular interest is the power deposition profile, as shown in figure 17. Both relativistic and non-relativistic simulations capture the partial ray damping far OA at the 2nd harmonic. Only the relativistic simulation captures the strong 1st

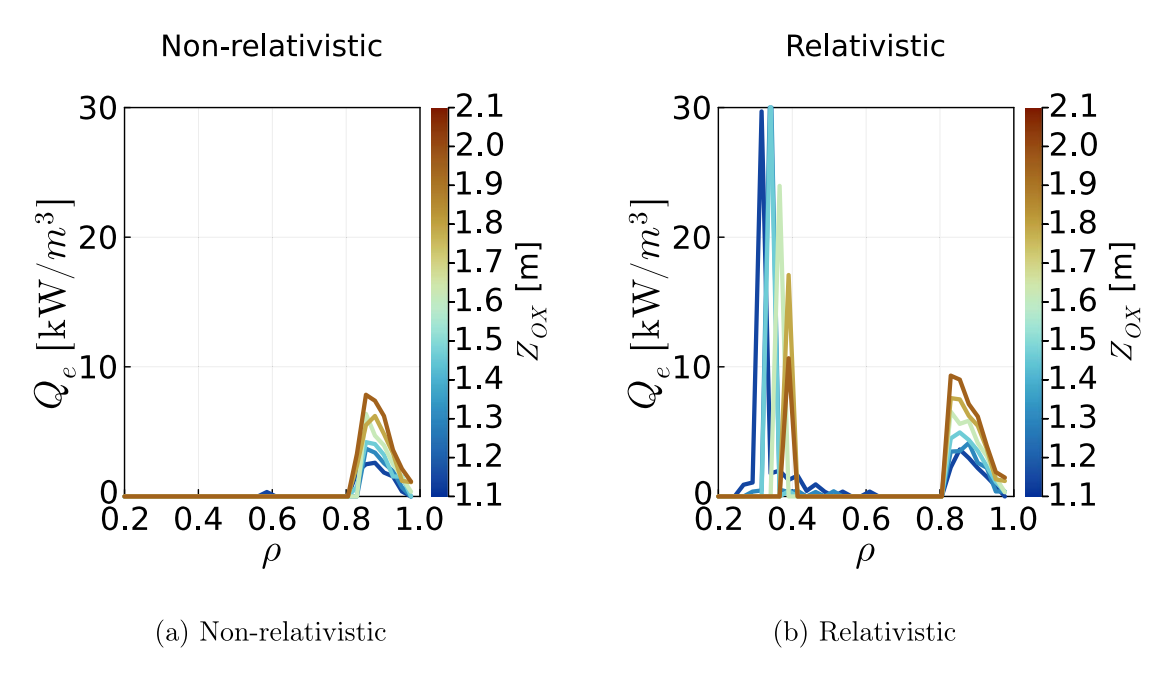


Figure 17. NA rays: power deposition profiles for 1 MW ray. f = 87 GHz. Near-axis power deposition (at  $\rho \approx 0.3$ ) is expected in both the non-relativistic and relativistic simulations. However, the non-relativistic rays terminate prematurely due to numeric errors.

harmonic damping near  $\rho = 0.3$ ; the non-relativisitic rays terminate prematurely due to numeric errors.

This numeric issue is related to that discussed in section 3. The relativistic rays make a low-field-side approach to the 1st harmonic and promptly damp all remaining power according to the relativistic damping model. The non-relativistic rays also approach the 1st harmonic but do not fully damp, at least according to the *mixed* damping model. They instead terminate prematurely with  $\sim 75\%$  of power un-damped. This is because the non-relativistic rays violate the weak-damping approximation well before the mixed-relativistic damping becomes significant. As a result, the rays begin propagating faster than light, causing the ray-tracer to terminate with an error.

The numeric issue discussed above prevents the non-relativistic ray-tracing of NA rays. These are also particularly interesting rays because they propagate so far into the plasma. Naturally, one hopes that relativistic ray-tracing will reveal high CD efficiencies close to the magnetic axis. This is unfortunately not the case, as small CD efficiencies of  $\eta \approx 0.001 \, \mathrm{A \, W^{-1}}$  are realised near-axis. In normalised units [29], this corresponds to  $\zeta_{\mathrm{CD}} \equiv 32 n_{20} R \eta_{\mathrm{A \, W^{-1}}} T_{\mathrm{keV}} \approx 0.08$ . These rays are strongly damped near the 'pinch-point,' the point at which the low-field-side resonance first becomes accessible (and then only for electrons with zero pitch angle). This point corresponds to:

$$n_{-}^{2}Y^{2} + N_{||}^{2} = 1 (11)$$

where  $n_{-}$  is the low-field-side harmonic (i.e.  $n_{-}=1$ ). Substituting this into the wave-particle resonance condition reveals that the pinch-point corresponds to resonant particles with  $v/v_{\rm te} = c|N_{||}|nY/(v_{\rm te}(1-N_{||}^2))$ , where  $v_{\rm te} = \sqrt{T_{\rm e}/m_{\rm e}}$ . Thus, resonant particle speed at the pinch-point is linearly

proportional to  $|N_{||}|$ . Given  $|N_{||}| \approx 0.2$  at the pinch-point (see figure 16), this corresponds to electron velocities of  $v/v_{te} \approx 1.5$ . These electrons are practically thermal, and therefore highly collisional and not attractive for driving current. One could therefore consider this an electron heating scheme.

Off axis (OA) rays: the 2nd class of rays are labelled OA rays because they deposit power in the region of  $0.4 < \rho < 0.7$  at the 2nd harmonic. Since these rays make a high-field-side approach to the cyclotron resonance, they are not susceptible to the same numeric issues plaguing NA rays in non-relativistic simulations. Nevertheless, there is a significant difference in ray trajectories between the non-relativistic and relativistic cases, as seen for launch above the mid-plane at 91 GHz (see figure 18). Again, the discrepancy starts to become noticeable at the X-B mode-conversion near the UHR.

At 91 GHz, both the relativistic and non-relativistic simulations predict a decrease in CD efficiency as  $Z_{OX}$  increases (see figure 19). There is, however, a quantitative mismatch in driven current. This mismatch grows as  $Z_{OX}$  increases and the power-deposition peak moves inwards. At  $Z_{OX} \approx +1.2$  m, the relativistic case predicts  $\sim 200\%$  higher CD efficiency (0.014 A W<sup>-1</sup> versus 0.0045 A/W).

Far Off Axis (FOA) rays: the 3rd class of rays are labeled FOA rays because they damp near the plasma edge ( $\rho > 0.7$ ). Figure 20 plots example ray trajectories for below mid-plane launch at f = 101 GHz. Once again, discrepancies between the relativistic and non-relativistic cases start to become noticeable at the X-B mode conversion. Concurrently, these rays undergo a large  $|N_{||}|$ -upshift. Hence, they very quickly damp in the edge. Given that these trajectories are relatively short, there is little *cumulative* disagreement between the relativistic and non-relativistic trajectories. In turn, there is

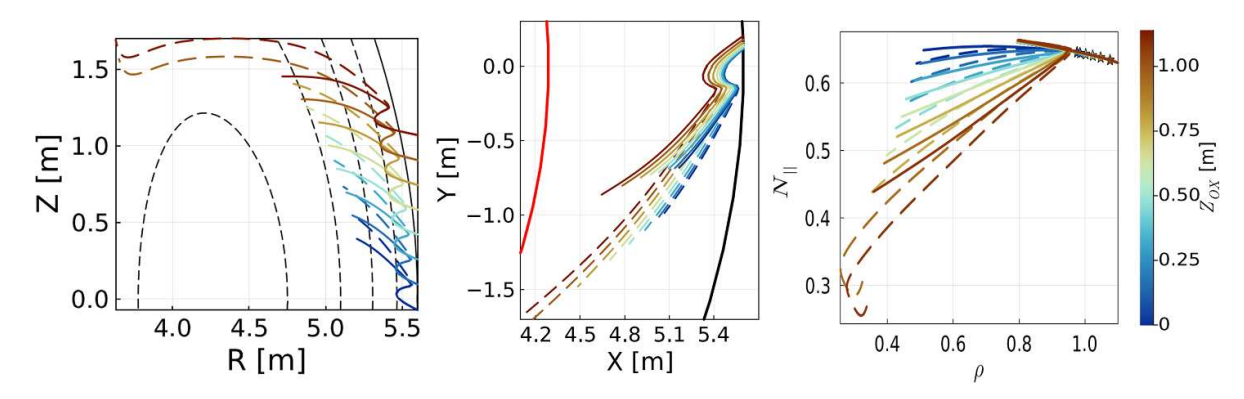


Figure 18. Off-axis (OA) rays at 91 GHz. Poloidal (left) and top-down (middle) projection of ray-trajectories. Right plot shows trajectories in phase-space. Solid: relativistic. Dashed: non-relativistic.

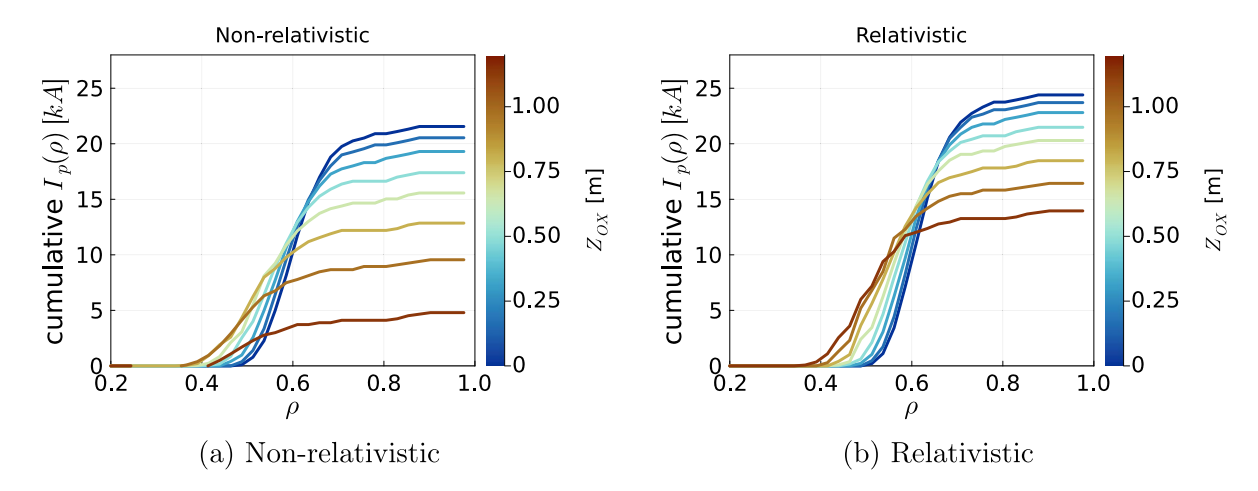


Figure 19. OA rays: cumulative driven current profile for 1 MW ray. Linear CD model used. f = 91 GHz.

little disagreement in the CD profiles (see figure 21). In other words, toroidal effects and Doppler broadening seem to overshadow the impact of relativistic propagation. Furthermore, these launch parameters predict a robust, high CD efficiency of  $\sim 0.03\,A~W^{-1}$  localised to  $\rho\approx 0.8$ .

#### 4.2. Quasilinear effects at high EBW power

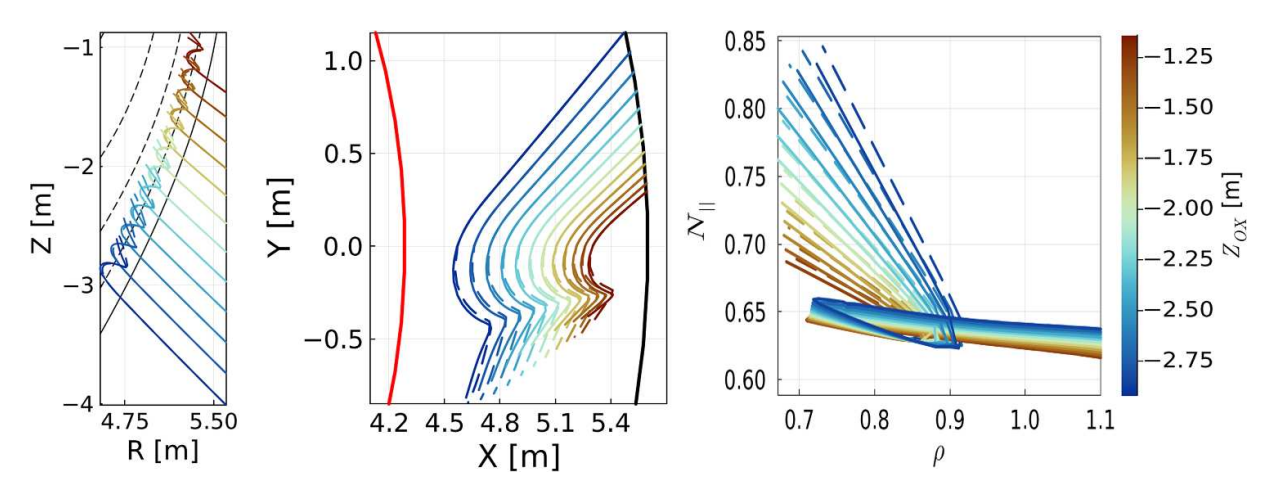
The linear CD model predicts maximum efficiency at  $f \approx 98$  GHz and  $Z_{\rm OX} \approx -1$  m. This corresponds to the FOA ray class, which suggests non-relativistic simulations are adequate. However, we have so far neglected quasilinear effects.

Quasilinearlity here refers to how CD efficiency is a function of power at sufficiently high power. This is caused by the EBW modifying the electron distribution away from a Maxwellian. Verification of the EBW linear CD model against CQL3D [19] reveals that quasilinear effects become important when  $\langle E \rangle / \sqrt{n_{19} \ln \Lambda / 16} \gtrsim 50 \text{V cm}^{-1}$ , where  $\langle E \rangle$  is the flux-surface averaged RF electric field amplitude,  $n_{19} \equiv n_{\rm e}/10^{19} {\rm m}^{-3}$ , and  $\ln \Lambda$  is the Coulomb logarithm [18]. This roughly translates to  $\gtrsim 1 \, {\rm MW}$  of launched EBW power in STEP. On the other hand,  $\gtrsim 100 \, {\rm MW}$  of EBW power is required for fully non-inductive steady state operation. It is therefore prudent to check how the conclusions above are impacted by quasilinearity.

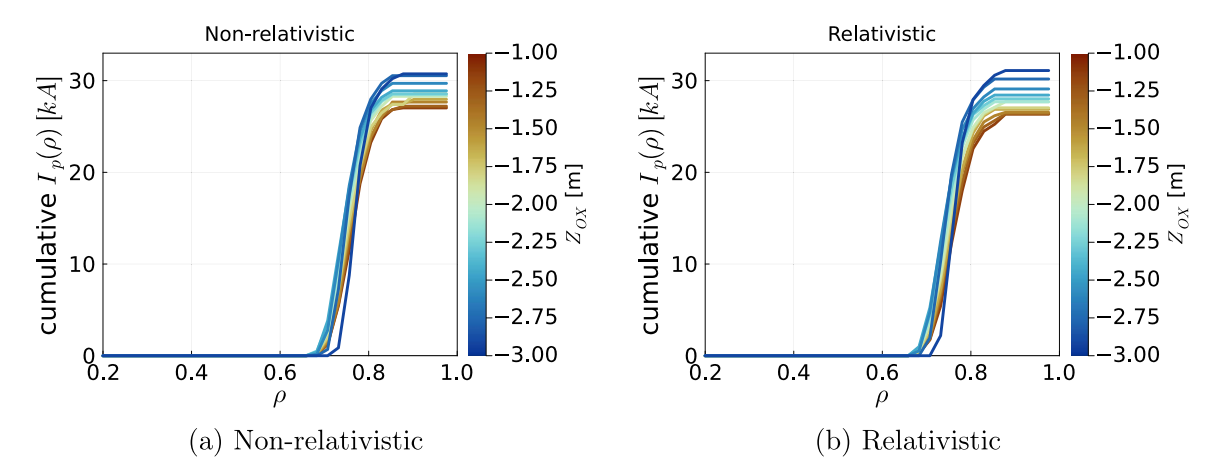
A ray-tracing scan in  $(f, Z_{\rm OX})$  is conducted around the linear optimal point. Then the ray trajectories are coupled to CQL3D for another scan in launched ray power. The power-scan is done for 1 kW, 1 MW, 10 MW, and 100 MW. Quasilinear effects are only noticeable at >1 MW. The result of this scan is presented in figures 22 and 23.

Figure 22 plots global CD efficiency  $(\eta)$  as a function of f,  $Z_{\rm OX}$ , and launched EBW power. At lower power ( $\leqslant 1$  MW), there is good agreement with the linear adjoint model. With increasing power (>1 MW), the optimal launch point is shifted to lower frequencies and larger  $Z_{\rm OX}$ . Assuming a 100 MW beam, the new optimal launch point is moved to 91 GHz and  $Z_{\rm OX} \approx -0.25$  m. Furthermore, at 100 MW, the *linear* optimal launch point sees a  $\sim 27\%$  decrease in  $\eta$ .

Figure 23 plots the radial location for maximum  $|j_{tor}|$  deposition. The general trend is for a radial shift inward as power increases. This is as expected, because the wave-particle interaction is a diffusive term that decreases  $|\nabla_{\bf v} f_e|$  at the resonance. In turn, wave damping will saturate at high powers, allowing for deeper penetration of the beam into the plasma. This effect is most noticeable for above mid-plane launch at 90–95 GHz, where the peak  $\rho$  shifts by -0.05 between the 1 MW and 100 MW case. Notably, the new optimal launch point corresponds to a peak deposition at  $\rho \approx 0.6$ . This is safely in the OA class of rays, indicating that relativistic effects are important.



**Figure 20.** Far off-axis (FOA) rays at 101 GHz. Poloidal (left) and top-down (middle) projection of ray-trajectories. Right plot shows trajectories in phase-space. Solid: relativistic. Dashed: non-relativistic.



**Figure 21.** FOA rays: cumulative driven current profile for 1 MW ray. Linear CD model used. f = 101 GHz.

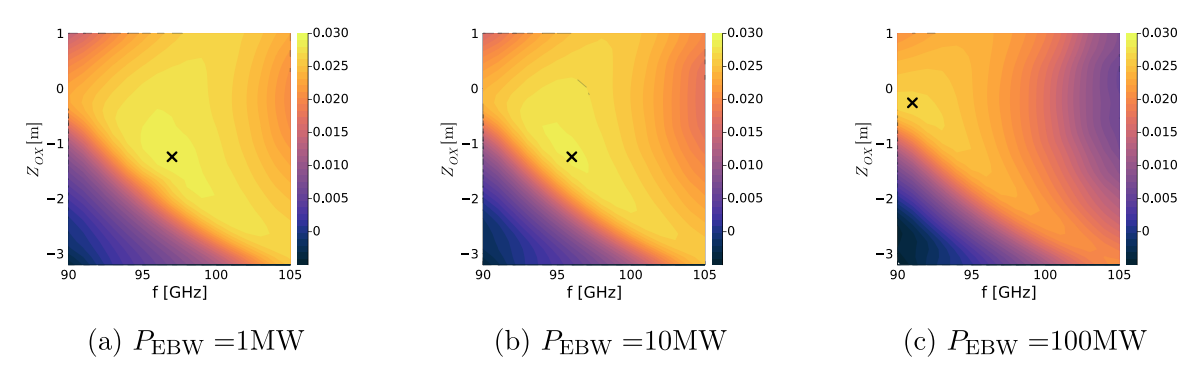


**Figure 22.** Global current drive efficiency  $\eta = I_{\text{CD}}/P_{\text{EBW}}$  [A W<sup>-1</sup>] as a function of frequency (f), launch height  $(Z_{\text{OX}})$ , and launched microwave power  $(P_{\text{EBW}})$ . Black cross indicates the optimal launch point at which  $\eta$  is maximised.

It should be emphasised that quasilinearity only impacts ray damping and the current response; it does not impact the ray trajectory. However, in taking account for quasilinear effects, the optimal launch point (that which maximised  $\eta$ ) is shifted from the FOA ray class to the OA ray class.

# 5. Summary

Efficient evaluation of the fully-relativistic hot dispersion, via the KK relations, enables fast EBW ray-tracing simulations in reactor-relevant plasmas. Such a ray-tracer is being applied to the optimisation of the EBCD launcher in STEP.

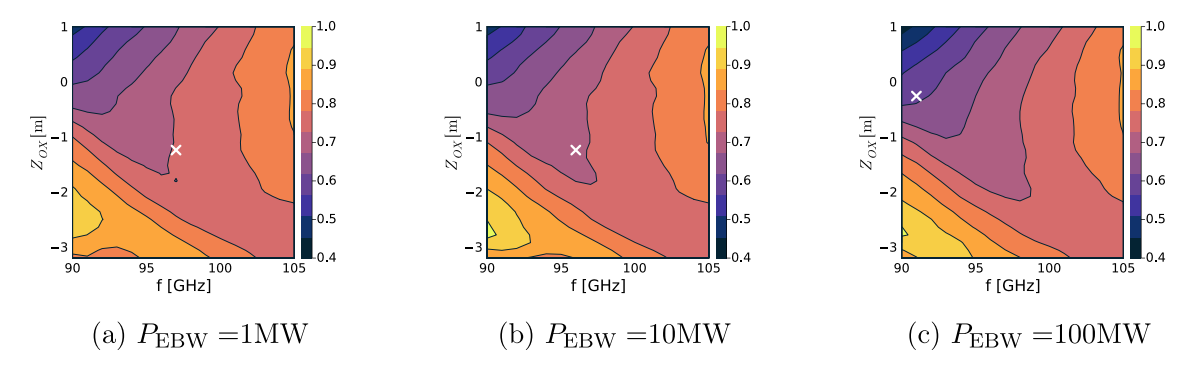


**Figure 23.** Radial location of peak current deposition as a function of frequency (f), launch height  $(Z_{OX})$ , and launched microwave power  $(P_{EBW})$ . White cross indicates the optimal launch point at which  $\eta$  is maximised.

Ray-traces of O-X-B mode-coupling in slab geometry verify that the KK dispersion exactly matches Trubnikov's 2nd Form, as it should. Slab runs indicate that relativistic modification to the ray trajectory becomes noticeable at the X-B mode-conversion and beyond. This effect grows with temperature. At  $T_{\rm e} \gtrsim 4\,{\rm keV}$ , one expects significant modification to the Bernstein wave. This is comparable to the pedestal temperature in STEP, and so further motivates the modelling of relativistic wave propagation in EBCD calculations.

Fully relativistic simulations of EBW ray propagation, damping, and current-drive have been conducted for a conceptual STEP steady-state operating point. To find all possible beam trajectories of interest, a 2D scan in frequency and poloidal launch height has been conducted. The parameter scan was restricted to outboard launch, and frequencies between 90 and 105 GHz to ensure efficient O-X-B coupling.

The relativistic EBCD simulations are compared against simulations in which ray-propagation is modelled in the nonrelativistic limit. In both cases, damping is modelled relativistically (see appendix B). Three particularly interesting classes of rays are identified. (1) Near-axis, or NA rays, propagate deep into the core and fully damp following a low-field-side approach of the 1st cyclotron harmonic. Relativistic effects weaken the low-field-side cyclotron resonance. In turn, nonrelativistic ray trajectories become un-physical prior to fully damping because the weak-damping approximation breaks down. Thus, these rays reveal a parameter regime in which relativistic simulations are essential. NA rays are only possible for above mid-plane launch because this corresponds to an initial  $|N_{||}$  down-shift. In turn, these rays avoid fully damping at the Doppler-broadened 2nd harmonic at larger  $\rho$ . Unfortunately, this  $|N_{||}$  downshift also results in poor CD efficiency at the 1st harmonic. (2) Off-axis, or OA rays, propagate to mid-radius before fully damping at the 2nd harmonic through a high-field-side approach. This coincides with a weak evolution in  $N_{||}$ . The high-field-side cyclotron resonance is strengthened through relativistic effects. Thus, issues with the weak-damping approximation in the non-relativistic limit are avoided. Nevertheless, significant disagreement in the ray trajectories and CD profiles persist. Thus, relativistic simulations are necessary for accurate predictions. (3) Far-off-axis, or FOA rays, refer to those with short trajectories that strongly damp at  $\rho > 0.7$  following a strong  $|N_{||}$  upshift. While the relativistic and non-relativistic trajectories start to diverge following the X-B conversion, the rays are too short for this to matter. A subset of these rays also exhibit high CD efficiency.

Linear parametric scans suggest that global CD efficiency is maximised near 98 GHz and  $Z_{\rm OX} = -1$  m, resulting in  $\eta \approx$  $0.03\,\mathrm{A\,W^{-1}},\,\mathrm{or}\,\,\zeta_{\mathrm{CD}}\approx0.6$  in normalised units. Current-drive would be localised to  $\rho \approx 0.75$ . This corresponds to the FOA class of rays, indicating relativistic propagation is not important at the optimal launch point. However, preliminary quasilinear modelling at reactor-relevant microwave powers indicate the optimal launch point will be shifted to lower frequencies and higher  $Z_{OX}$ . In turn, the current peak is pushed inwards to  $\rho \approx 0.6$ . This corresponds to the OA class of rays, for which relativistic effects can significantly modify CD performance. We also note that, at this particular operating point with 100 MW of EBW power, the new optimal launch point also results in  $\eta \approx 0.03$ A W<sup>-1</sup>, but a slightly lower  $\zeta_{CD} \approx 0.55$ . This would enable the non-inductive drive of 4 MA with around 130 MW of injected power. Quasilinear predictions will be further explored in a future paper.

At low powers, the optimal region in  $(f, Z_{OX})$ -space is fairly broad (see figure 23(b)), which indicates it is insensitive to small changes in launcher design and plasma parameters. At high powers (see figure 23(c)), the optimal region shrinks, indicating that CD performance is relatively less robust. Strictly speaking, the O-X coupling window must also be taken into account. That is a separate—albeit important—consideration and is outside the scope of this work.

Three large caveats must be explicitly stated about the conclusions drawn above. First, these simulations assume perfect O-X-B mode-conversion by virtue of enforcing the optimal  $N_{||}$  at the O-mode cutoff. In reality, full-wave effects, including finite beam width, will result in a mode-conversion efficiency that is less than unity. Thus, full-wave calculations of the mode-conversion window are required to understand how practical each launch point really is. Second, the plasma parameters have been kept fixed. It would be prudent to determine how CD performance changes as a result of small variations to the plasma equilibrium. The work herein has developed a method for solving fully-relativistic ray trajectories in minutes, as opposed to hours. This speed-up will further facilitate these parametric scans. Lastly, it is worthwhile to consider that the quasilinear treatment of the wave-particle

resonance may be invalid, especially for high-power, highly localized microwave beams [30]. This consideration is outside the scope of this paper, but important to address in future work.

Lastly, one must comment on the necessity of relativistic ray-tracing in present-day devices. The model described in this paper was applied to a typical MAST-U discharge ( $T_{\rm e0} \approx 2~{\rm kev}$ ) for near-axis current-drive. The error in non-relativistic rays was negligible. High temperature ( $T_{\rm e} \gtrsim 4~{\rm keV}$ ) is necessary, but not sufficient, for a large relativistic impact. As demonstrated in this paper, ray length is also a factor.

# Acknowledgment

This work has been funded by STEP, a UKAEA programme to design and build a prototype fusion energy plant and a path to commercial fusion.

#### Conflict of interest

The authors report no conflict of interest.

# Appendix A. Details of ray propagation

Propagation is modelled via the well-known geometrical optics equations [21]:

$$\frac{\mathrm{d}\mathbf{r}}{\mathrm{d}t} = -\frac{\partial D^{H}(\mathbf{r}, \mathbf{k}, \omega) / \partial \mathbf{k}}{\partial D^{H}(\mathbf{r}, \mathbf{k}, \omega) / \partial \omega}$$
(A.1a)

$$\frac{\mathrm{d}k}{\mathrm{d}t} = \frac{\partial D^{H}(\mathbf{r}, \mathbf{k}, \omega) / \partial \mathbf{r}}{\partial D^{H}(\mathbf{r}, \mathbf{k}, \omega) / \partial \omega}$$
(A.1b)

where  $D^H$  is the Hermitian component of the dispersion relation (a.k.a. the ray Hamiltonian). Heuristically, ray-tracing is valid as long as the wavelength is much shorter than the characteristic length scale of the plasma. The weak-damping condition  $(|Im(k_\perp)| \ll R(k_\perp))$  must also be satisfied. The above equations are solved using a 4th order Runge-Kutta scheme.

In the slab geometry of section 3, the ray-tracing equations are solved in Cartesian coordinates (x, y, z) and  $(k_x, k_y, k_z)$ . Since the plasma is homogeneous in the y and z direction, it follows that  $k_y$  and  $k_z$  are constant.

In the toroidal geometry of section 4, the ray-tracing equations are solved in cylindrical coordinates  $(R, \phi, Z)$  and  $(k_R, k_\phi, k_Z)$ . Since the plasma is assumed axisymmetric (homogeneous along  $\phi$ ), it follows that  $Rk_\phi$  is constant.

#### Appendix B. Details of ray damping

The perpendicular damping coefficient along a ray is proportional to  $\text{Im}(k_{\perp})$ , which is calculated via the weak-damping approximation

$$\operatorname{Im}(k_{\perp}) \approx -\frac{D^{AH}}{\partial D^{H}/\partial k_{\perp}} \bigg|_{k_{\perp} = R(k_{\perp})}$$
 (A.2)

where  $D^H$  is the Hermitian part of the Hamiltonian, and  $D^{AH}$  is the anti-Hermitian part. One advantage of the above approximation is that the Hermitian and anti-Hermitian terms are un-coupled. The denominator in the right-hand side of equation (A.2) is sensitive to how close  $R(k_{\perp})$  is to the root of  $D^H$ . Since the ray-tracing equations provide  $R(k_{\perp})$ , the choice of  $D^H$  in equation (A.2) should match equation (A.1). The choice of  $D^{AH}$  is usually less critical. In this paper, relativistic simulations refer to the use of the relativistic dispersion in both the numerator and denominator. This is self-consistent. For non-relativistic ray trajectories, one can either use the nonrelativistic dispersion everywhere, or take a 'mixed' approach. In the mixed approach, one uses the non-relativistic  $D^H$  and the relativistic  $D^{AH}$ . This allows one to account for relativistic damping along non-relativistic trajectories. This is computationally efficient and therefore a common technique in other codes, like GENRAY [31]. However, this approach has serious shortcomings as the ray approaches the low-field side harmonic resonance in hot plasmas, as discussed in sections 3 and 4.

#### **ORCID iDs**

#### References

- [1] Laqua H.P. 2007 Electron Bernstein wave heating and diagnostic *Plasma Phys. Control. Fusion* **49** R1–R42
- [2] Wilson T., Freethy S., Henderson M., Köhn-Seemann A., Konoplev I., Saarelma S., Speirs D. and Vann R. (the STEP team) 2023 Electron Bernstein Wave (EBW) current drive profiles and efficiency for STEP EPJ Web of Conf. vol 277 p 01011
- [3] Freethy S. *et al* (the STEP team) 2023 Microwave current drive for STEP and MAST Upgrade *EPJ Web of Conf.* vol 277 p 04001
- [4] Tholerus E. *et al* (the STEP team) 2024 Flat-top plasma operational space of the STEP power plant *Nucl. Fusion* **64** 106030
- [5] Taylor G., Efthimion P.C., Kessel C.E., Harvey R.W., Smirnov A.P., Ershov N.M., Carter M.D. and Forest C.B. 2004 Efficient generation of noninductive, off-axis, Ohkawa current, driven by electron Bernstein waves in high β, spherical torus plasmas *Phys. Plasmas* 11 4733–9
- [6] Urban J., Decker J., Peysson Y., Preinhaelter J., Shevchenko V., Taylor G., Vahala L. and Vahala G. 2011 A survey of electron Bernstein wave heating and current drive potential for spherical tokamaks *Nucl. Fusion* 51 083050
- [7] Ram A.K., Decker J. and Peysson Y. 2005 On electron Bernstein waves in spherical tori *J. Plasma Phys.* **71** 675
- [8] Trubnikov B. 1959 Plasma Physics and the Problem of Controlled Thermonuclear Reactions Vol III (Permagnon)
- [9] Weiss I. 1985 Electromagnetic wave propagation in relativistic magnetized plasmas *J. Comput. Phys.* **61** 403–16
- [10] Decker J. and Ram A.K. 2006 Relativistic description of electron Bernstein waves *Phys. Plasmas* 13 112503
- [11] Nelson-Melby E., Harvey R.W., Smirnov A.P. and Ram A.K. 2007 Relativistic ray-tracing of electron Bernstein waves in a spherical tokamak reactor *Plasma Phys. Control. Fusion* 49 1913–29

- [12] Airoldi A.C. and Orefice A. 1982 Relativistic dielectric tensor of a Maxwellian plasma for electron cyclotron waves at arbitrary propagation angles J. Plasma Phys. 27 515–24
- [13] Shkarofsky I.P. 1986 New representations of dielectric tensor elements in magnetized plasma *J. Plasma Phys.* 35 319–31
- [14] Swanson D.G. 2002 Exact and moderately relativistic plasma dispersion functions *Plasma Phys. Control. Fusion* 44 1329–47
- [15] Saveliev A.N. 2005 Approximate relativistic dispersion relation for electron Bernstein waves in a Maxwellian plasma *Plasma Phys. Control. Fusion* 47 2003–17
- [16] Volpe F. 2007 Weakly relativistic dielectric tensor for arbitrary wavenumbers *Phys. Plasmas* 14 122105
- [17] Pavlov S. and Castejon F. 2018 The fully relativistic dielectric tensor for arbitrary wave vectors *Nucl. Fusion* 58 126030
- [18] Biswas B., Speirs D., Freethy S. and Vann R. 2023 Application of linear electron Bernstein current drive models in reactor-relevant spherical tokamaks *Nucl. Fusion* 63 126011
- [19] Harvey R.W. and Mccoy M.G. 2005 The CQL3D Fokker-Planck Code (reconstituted in editable form from General Atomics Report GA-A20978, 1992) Technical Report
- [20] Swanson D.G. 2003 Plasma Waves Series in Plasma Physics 2nd edn (Institute of Physics Pub)
- [21] Stix T.H. 1992 Waves in Plasmas (Springer)
- [22] Kramers H. 1927 La diffusion de la lumiere par les atomes Atti Cong. Intern. Fisica (Trans. of Volta Centenary Congress) 2 545–57

- [23] Kronig R. 1926 On the theory of dispersion of x-rays *J. Opt. Soc. Am. A* **12** 547–57
- [24] Brambilla M. 1998 Kinetic Theory of Plasma Waves: Homogeneous Plasmas (Oxford University Press)
- [25] Diem S.J., Taylor G., Caughman J.B., Efthimion P.C., Kugel H., LeBlanc B.P., Phillips C.K., Preinhaelter J., Sabbagh S.A. and Urban J. 2009 Collisional damping of electron Bernstein waves and its mitigation by evaporated lithium conditioning in spherical-tokamak plasmas *Phys.* Rev. Lett. 103 015002
- [26] Laqua H.P., Erckmann V., Hartfuß H.J. and Laqua H. 1997 Resonant and nonresonant electron cyclotron heating at densities above the plasma cutoff by O-X-B mode conversion at the W7-As stellarator *Phys. Rev. Lett.* 78 3467–70
- [27] Fisch N.J. and Boozer A.H. 1980 Creating an asymmetric plasma resistivity with waves *Phys. Rev. Lett.* 45 720–2
- [28] Ohkawa T. 1976 General Atomics Report GA-A13847 General Atomics (available at: https://library.psfc.mit.edu/ catalog/online\_pubs/tech\_reports/GA-A13847.pdf)
- [29] Luce T.C., Lin-Liu Y.R., Harvey R.W., Giruzzi G., Politzer P.A., Rice B.W., Lohr J.M., Petty C.C. and Prater R. 1999 Generation of localized noninductive current by electron cyclotron waves on the DIII-D tokamak *Phys.* Rev. Lett. 83 4550–3
- [30] Kamendje R., Kasilov S.V., Kernbichler W. and Heyn M.F. 2003 Kinetic modeling of nonlinear electron cyclotron resonance heating *Phys. Plasmas* 10 75–97
- [31] Smirnov A. and Harvey R. 2001 The GENRAY ray tracing code *Technical Report* CompX